Journal of Materials Science & Technology 297 (2027) 44–52

Contents lists available at ScienceDirect

Journal of Materials Science & Technology

journal homepage: www.elsevier.com/locate/jmst

Research Article

Enhancing hydrogen storage performance of porous carbon materials by co-doping B and N combined with pore texture tuning

Zeming Zhong[a], Xue Gao[a,c], Yuchen Mao[a,d], Hui Wang[a], Yujun Zhao[b], Lan Zhang[e,f,g], Min Zhu[a,e,*]

[a] School of Materials Science and Engineering, Key Laboratory of Advanced Energy Storage Materials of Guangdong Province, South China University of Technology, Guangzhou 510640, China
[b] School of Physics and Optoelectronics, Key Laboratory of Advanced Energy Storage Materials of Guangdong Province, South China University of Technology, Guangzhou 510640, China
[c] Foshan Power Supply Bureau, Guangdong Power Grid Corp, Foshan 528010, China
[d] Institute of Advanced Materials and Technology, Guangdong University of Technology, Guangzhou 510006, China
[e] Energy Research Institute @NTU, Nanyang Technological University, 50 Nanyang Avenue, Singapore 637553, Singapore
[f] China-Singapore International Joint Research Institute (CSIJRI), Guangzhou Knowledge City, Guangzhou 510663, China
[g] State Key Laboratory of Thorium Energy, Shanghai Institute of Applied Physics, Chinese Academy of Sciences, Shanghai 201800, China

ARTICLE INFO

Article history:
Received 25 August 2026
Revised 1 November 2026
Accepted 1 November 2026
Available online 10 November 2026

Keywords:
Hydrogen storage
Physisorption
Porous carbon materials
Boron and nitrogen co-doping
Activation process

ABSTRACT

Porous carbon materials (PCMs) are promising for hydrogen storage due to their low cost, tunable texture, high capacity, and superior kinetic performance, yet their low isosteric heat of adsorption limits practical applications. Heteroatom doping can enhance the interaction between C substrates and H_2 molecules, but the specific surface area (SSA) is generally greatly reduced by the activation process required for doping. Thus, the hydrogen storage performance of PCMs is still poor after doping. In this study, high SSA (2346 m^2/g) and co-doping efficiency have been simultaneously achieved for the PCM sample by tuning the activation process. Therefore, the hydrogen storage performance is greatly promoted owing to high SSA and the synergistic effect of co-doped B and N. The gravimetric, volumetric, and usable hydrogen storage capacities are 4.25 wt.%, 27.02 g/L, and 11.44 g/L (1.5–50 bar), respectively, for this B and N co-doped PCM at 77 K and 50 bar. Even at 298 K, its gravimetric hydrogen storage capacity reached 1.50 wt.%, surpassing that of the commercial AB_5 alloy. Density functional theory calculations show B and N meta-co-doped substrate (B1CN1) has higher single H_2 adsorption energy (−7.83 kJ/mol) than either B-doped (BC1, −6.61 kJ/mol) or N-doped (CN1, −7.34 kJ/mol) substrate. Additionally, increasing the B/N ratio in the range of B/N < 1 increases charge defects, enhancing H_2 adsorption on the C substrate. This study not only reveals the synergistic effect of co-doped B and N but also demonstrates the importance of achieving a balance between doping and the texture of PCMs, providing valuable insights for developing high-performance PCMs for hydrogen storage.

© 2026 Published by Elsevier Ltd on behalf of The editorial office of Journal of Materials Science & Technology.

1. Introduction

High-capacity, reversible, and efficient hydrogen storage under safe and mild conditions is still one of the key challenges for large-scale application of clean hydrogen energy [1,2]. Physisorption hydrogen storage materials (PHSMs) have emerged as a promising candidate due to their high theoretical hydrogen storage capacity, excellent adsorption-desorption kinetics, and cycling performance [3]. Nevertheless, the weak Van der Waals interactions between H_2 molecules and PHSMs, with adsorption enthalpy being 4–10 kJ/mol, severely hinder practical applications [4]. Therefore, it is of great importance to develop PHSMs with both high H_2 adsorption enthalpy and storage capacity. Among various PHSMs, porous carbon materials (PCMs) have become a focus in hydrogen storage technology due to their high specific surface area (SSA), low cost, and ease of modification [5,6].

Currently, strategies to enhance the H_2 adsorption enthalpy of PCMs primarily include optimizing pore structure and doping with either heteroatoms or metal atoms. For instance, tuning the pore size to match the kinetic diameter of H_2, which is 0.4–0.6 nm, can strengthen the potential field of pore walls, thereby increasing H_2 adsorption enthalpy [7,8]. However, precise control of pore

* Corresponding author.
E-mail address: memzhu@scut.edu.cn (M. Zhu).

https://doi.org/10.1016/j.jmst.2026.11.010
1005-0302/© 2026 Published by Elsevier Ltd on behalf of The editorial office of Journal of Materials Science & Technology.

size at the nanoscale has limited effect, in addition to its complicated process that challenges large-scale production [9,10]. In contrast, doping offers considerable scope for tuning the adsorption enthalpy and is more feasible for large-scale production. Metal doping, such as alkali metals (Li, Na, and Mg) [11–13], transition metals (Ti, Mn, and V) [14–16], and noble metals (Pd, Pt, and Ru) [17–19], can significantly increase H_2 adsorption enthalpy through mechanisms of molecular polarization, Kubas interaction, and hydrogen spillover, respectively. However, these approaches often suffer from poor stability of the metal-substrate interface and high costs when noble metals are used [20]. Heteroatom doping offers a cost-effective method to enhance H_2 adsorption strength by inducing charge density distortions in PCMs, making it a highly promising strategy [21,22].

Nitrogen, due to its similarity to carbon in atomic radius, has been extensively studied as a dopant. By density functional theory (DFT) calculations, Petrushenko et al. found that the calculated adsorption energy (E_{ads}) of N-pyrrole graphene and 2N-graphene (−5.78 and −5.23 kJ/mol, respectively) was higher than that of pristine graphene (−3.85 kJ/mol), theoretically confirming the enhancement effect of N doping on H_2 adsorption [23]. Numerous experimental studies support this conclusion. For example, Kang et al. synthesized N-doped carbon aerogels with a maximum hydrogen storage capacity of 3.2 wt.% at 77 K and 20 bar, representing a 72% increase over undoped samples [24]. Similarly, N-doped microporous and mesoporous carbon materials exhibited 83% and 18% increases in hydrogen storage capacity at room temperature, respectively [25,26]. Additionally, N doping improves H_2 adsorption enthalpy, as evidenced by the increase in the isosteric heat of adsorption (Q_{st}) of NHPC-*x* from 7.45 to 7.95 kJ/mol and NPC-*XY* from 6.94 to 9.74 kJ/mol with increasing N content [27]. However, the activation process of N doping leads to a great loss of SSA in all those reported works, thereby reducing hydrogen storage capacity [27–29]. Thus, balancing doping levels and SSA is crucial during the preparation of PCMs.

Boron, another commonly used dopant, theoretically enhances the interaction between H_2 molecules and C substrates by introducing electron-deficient sites [30,31]. Firlej et al. demonstrated through first-principles calculations that the minimum interaction energy between H_2 and B in a pyrene-simulated graphene layer ($E_{ads(B\text{-}H2)} = -7.8$ kJ/mol) was 50% higher than that of the undoped graphene [32]. Experimentally, Chung et al. prepared microporous B-doped PCMs (B/C-II-600) and achieved a hydrogen storage capacity of 3.2 wt.% at 77 K and 60 bar, nearly double that of their pure carbon counterparts, along with a high Q_{st} (∼11 kJ/mol) [33]. Similarly, Qajar et al. found that after depositing BC_x on AC, the Q_{st} rose from 9 to over 14 kJ/mol and the H_2 uptake per SSA at room temperature and 100 bar increased from 0.245×10^{-3} to 1.572×10^{-3} wt.% g/m^2, indicating that B doping can enhance surface H_2 absorption ability [34]. Like N doping, the efficacy of B doping is also activation-dependent, highlighting the necessity of rational activation optimization [35].

Compared to single-element doping, the effect of B and N co-doping on PCMs is controversial, and their mechanisms remain unclear. Escalona et al. treated commercial activated carbon with ammonia and borax decahydrate and found that B and N co-doped samples exhibited lower hydrogen storage capacities than those doped with each element alone, with no observed synergistic effect [36]. In contrast, significant improvements were reported in hydrogen storage performance through B and N co-doping. For instance, borax-modified N-doped activated carbon showed a 76% increase in hydrogen storage capacity at −196 °C [37], while B_2O_3-modified PCMs achieved a 53% improvement in room temperature hydrogen storage capacity compared to PCMs with similar SSA [38]. However, the synergistic mechanism of B and N co-doping has not been thoroughly explored. While B and N doping individually introduce electron-deficient and electron-rich centers, respectively, the formation of a Bδ$^+$-Nδ$^-$ structure through co-doping may further disrupt charge distribution uniformity, thereby enhancing the interaction between the C substrate and H_2 molecules [39]. Similar to single-element doping, the activation process influences the doping amount efficiency and microstructure, such as pore size and SSA, of B and N co-doped PCMs [40,41]. Therefore, optimizing the activation process is critical for achieving better hydrogen storage performance of B and N co-doped PCMs.

Based on the above insights, this work fabricates B and N co–doped PCMs (BNCs) via one–step activation. Tuning activation temperature, activator dosage, and duration optimizes their surface chemistry and microstructure to improve hydrogen storage performance. Combined experimental and theoretical results reveal that B–N co–doping strengthens H_2 adsorption on carbon frameworks, yielding a synergistic enhancement in hydrogen storage. This study provides a feasible strategy for developing high–performance heteroatom–doped PCMs by balancing doping content and SSA.

2. Experimental section

2.1. Preparation of BNC, BC, NC, and C

Detailed chemical and material information is provided in Text S1 in the Supplementary Materials. Fig. 1(a) schematically depicts the synthetic route for BNCs. Briefly, 4–formylphenylboronic acid (FPBA) and p–phenylenediamine (PPD) were dissolved in 1,4–dioxane/mesitylene (1:1, v/v). After sonication, the mixture reacted at 120 °C for 3 days. The precipitate was filtered and Soxhlet–extracted with dichloromethane to afford the FPBA–PPD polymer (FPP). FPP was ground with a mild $CuBr_2$ activator, which avoids over-etching of the precursor, and carbonized under an Ar atmosphere (3 °C min^{-1}) at varied temperatures and durations. The product was H_2SO_4–H_2O_2 treated, washed, and vacuum–dried at 120 °C to obtain BNC–*T*–*n*–*t* (*T*: activation temperature, *n*: activator dosage, *t*: activation time). For comparison, mono-doped BC–800–10–2, NC–800–10–2, and undoped C–800–10–2 were prepared following the analogous synthetic route of BNCs, with only monomer precursors substituted. Specifically, FPBA was replaced by 4-formylbenzoic acid for NC–800–10–2, whereas both FPBA and PPD were substituted with 1,4-phenylenebisboronic acid for BC–800–10–2, and poly(divinylbenzene) was directly used as the precursor for C-800-10-2.

2.2. Materials characterization

Fourier–transform infrared (FTIR) spectroscopy (Nicolet IS50) probed chemical bonds of BNCs. Surface chemical states were analyzed by X-ray photoelectron spectroscopy (XPS, Escalab Xi+), calibrated against C 1s (284.8 eV) and fitted via Avantage software. Elemental contents (C and N) were obtained by Elementar Vario EL (CNHS mode). Scanning electron microscope coupled with energy–dispersive X–ray spectroscopy (SEM–EDS), transmission electron microscope (TEM)–EDS, and X-ray diffraction (XRD, Cu–Kα, 45 kV, 40 mA) characterized morphology and microstructure. Raman spectroscopy (514.5 nm laser, 40 mW, Origin 2021 Gaussian fitting) evaluated structural disorder. N_2 sorption isotherms (77 K, Quantachrome Autosorb–iQ) were recorded after 300 °C–8 h degassing. BET SSA, total pore volume (V_{total}), micropore volume (V_{micro}), and NLDFT pore size distribution (PSD) were derived. Skeleton and packing densities were determined on a Sieverts–type BSD–pH 200 instrument with He–volume calibration.

2.3. Hydrogen storage performance testing

Low-pressure hydrogen adsorption isotherms (0–1 bar) of the samples were measured at 77 and 87 K using a Quantachrome Autosorb-iQ gas adsorption analyzer. High-pressure hydrogen adsorption tests were conducted at 77 K (0–50 bar), 223 K, and 298 K (0–130 bar) on a Sieverts-type BSD-pH 200 instrument. All samples were vacuum degassed at 300 °C for 8 h in advance, and high-purity hydrogen (99.999%) was applied throughout the tests. The true gravimetric hydrogen storage capacity was corrected from the excess adsorption data obtained at 77 K, and the adsorbed phase density was fitted via the Langmuir-Freundlich equation [42]. The volumetric hydrogen storage capacity was further calculated based on the gravimetric capacity and sample packing density. The isosteric heat of adsorption was determined by fitting hydrogen adsorption isotherms at four different temperatures with the virial equation [43], using fixed fitting coefficients for accurate calculation of adsorption enthalpy.

2.4. First-principles calculations

All DFT calculations were carried out using the Vienna ab initio Simulation Package. Detailed calculation methods and parameters are provided in Text S2.

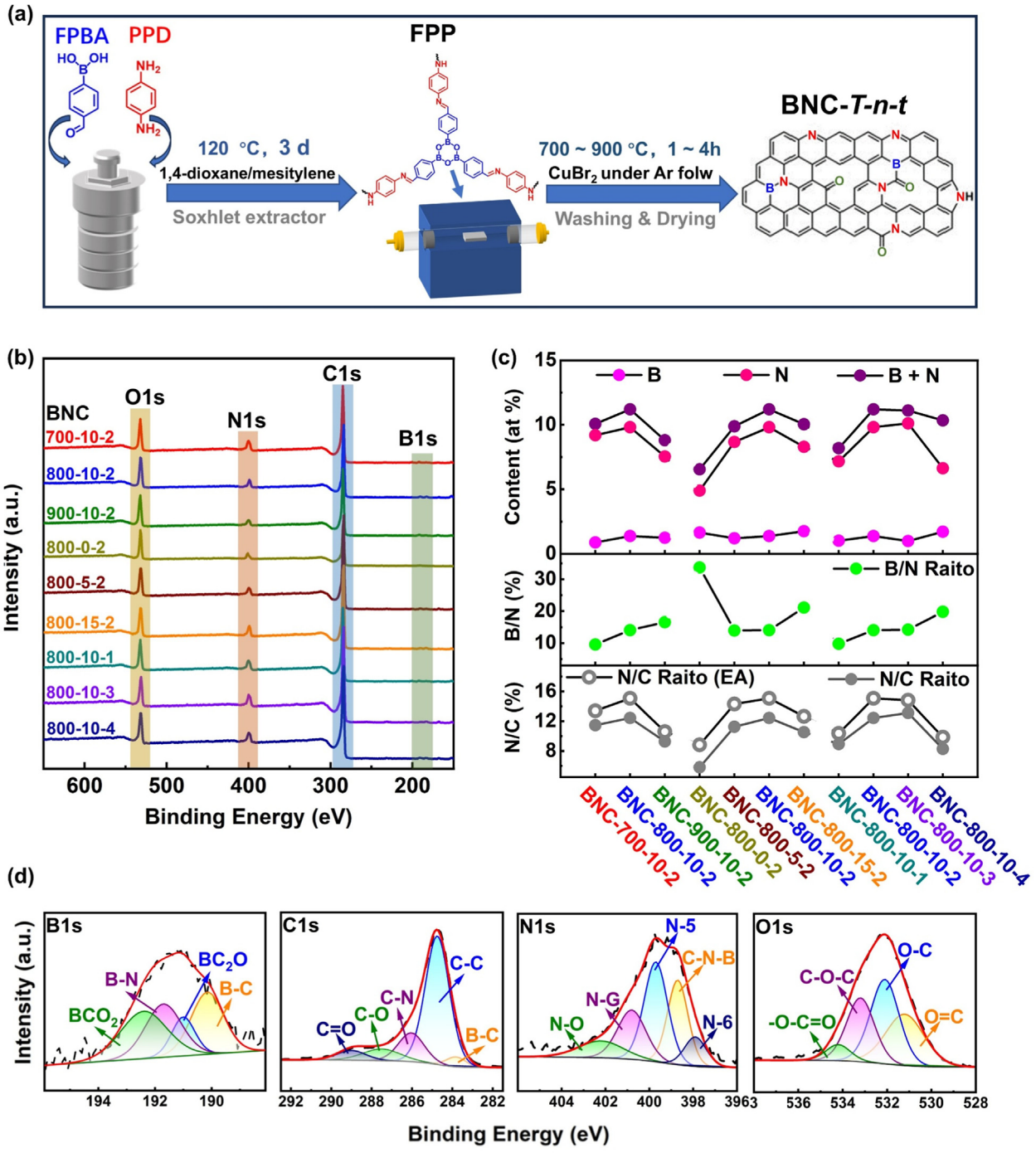

Fig. 1. (a) The synthesis route of BNCs. (b) The full XPS survey spectra and (c) the contents of B, N, and B+N and the ratios of B/N and N/C for BNCs prepared at different activation conditions. (d) B 1s, C 1s, N 1s, and O 1s high-resolution XPS spectra of BNC-800-10-2 samples.

3. Results and discussion

3.1. Effect of activation conditions on the surface chemical state of BNCs

The effects of activation processes on the surface chemical states of BNCs were systematically investigated via XPS, FTIR, and elemental analysis (EA). The XPS survey spectra (Fig. 1(b)) display characteristic C 1s, N 1s, O 1s, and weak B 1s peaks, verifying the successful coexistence of B, N, C, and O elements in BNCs. FTIR spectra (Fig. S1) exhibit typical stretching vibrations of C-B, C-N, and B-N bonds, confirming the effective incorporation of B and N into carbon skeletons [44]. EA (Table S1) shows that the B content of most samples is below 2.0 at.%, much lower than the N content above 7.0 at.%, which is attributed to the low B proportion in the FPP precursor and the difficult formation of stable B-C bonds. As illustrated in Fig. 1(c), the N content presents an upward-then-downward trend with intensified activation. Mild activation promotes precursor decomposition and preliminary carbonization, while moderate activation facilitates graphitization and nitrogen embedding to increase N doping. Excessively harsh activation causes gradual nitrogen desorption and reduced N content.

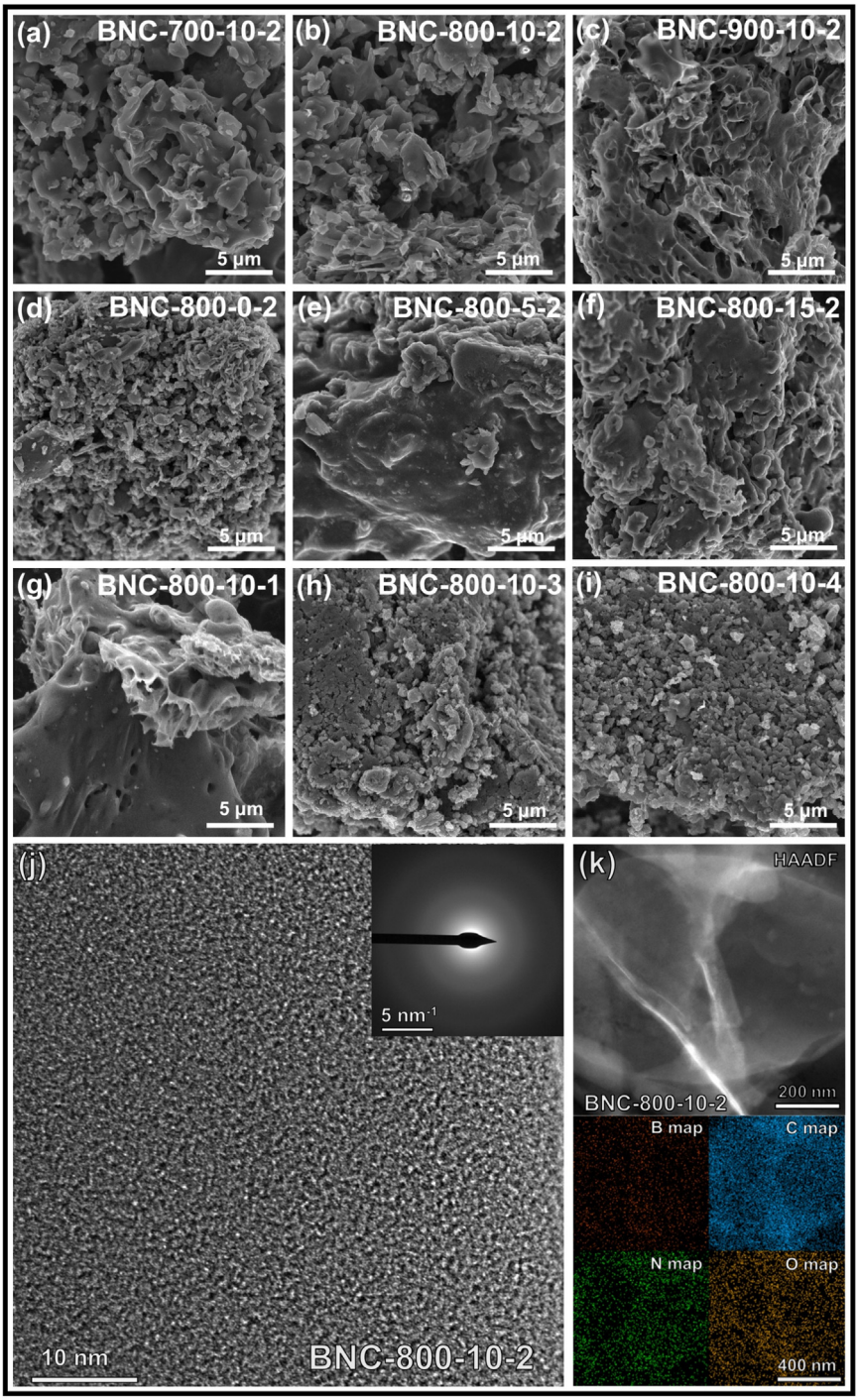

Fig. 2. (a–i) SEM images of BNCs prepared at different activation conditions. (j) HRTEM image and SAED pattern and (k) HAADF image and corresponding EDS of BNC-800-10-2.

By contrast, the B content remains stable at 1.0 at.%–2.0 at.%, yielding an elevated B/N ratio under intense activation. The highly consistent N/C ratios from XPS and EA verify the reliability of XPS for evaluating the overall elemental composition of BNCs. High-resolution Lorentz-Gaussian fitting of B 1s, C 1s, and N 1s spectra for BNC-800-10-2 (Fig. 1(d)) further reveals detailed heteroatomic chemical states [40,41]. The deconvoluted C 1s peaks confirm the formation of C-C, C-B, C-N, C-O, and C=O bonds. Fitted N 1s spectra contain pyridinic N, C-N-B, pyrrolic N, graphitic N, and oxidized N. Specifically, pyrrolic and pyridinic N serve as electron donors and active adsorption sites, while graphitic N optimizes surface charge density. B 1s fitting identifies B-C, B-N, BC_2O, and BCO_2 configurations, enabling stable B doping. Similar fitting results for other samples are provided in Fig. S2. All BNCs exhibit relatively high oxygen contents (~10 at.%), which originate from residual oxygen-containing groups in the precursor and oxygen introduced during acid washing. The BNCs show similar oxygen contents, and oxygen species mainly exist as edge functional groups, leading to a consistent influence of oxygen on surface properties. Thus, differences in B and N co-doping dominate the modulation of material surface properties.

3.2. Effect of activation conditions on the microstructure of BNCs

The effects of activation conditions on BNC surface morphology were investigated via SEM (Fig. 2(a–i)). Activation temperature exerts a dominant influence on microstructure. $CuBr_2$ etching transforms lamellar FPP (Fig. S3) into porous nanosheets at 700 °C. Moderate heating to 800 °C yields thinner, loose, and flocculent nanosheets, while excessive heating at 900 °C induces structural hollowing, loosening, and collapse, causing severe structural degradation. The activator dosage and activation time also regulate morphology. Activator-free samples present fragmented particles, while low activator dosage produces bulky blocks. Excessive activator creates abundant hollow pores, analogous to the high-temperature etching effect. Short activation time leads to unoptimized blocky structures, whereas prolonged treatment triggers gradual sheet fragmentation and severe structural collapse.

TEM characterization of BNC-800-10-2 further clarifies the microstructure (Fig. 2(j)). High-resolution TEM (HRTEM) images reveal uniform worm-like micropores and featureless lattice fringes, together with diffuse selected-area electron diffraction (SAED) rings confirm the amorphous carbon structure, consistent with XRD results (Fig. 3(a)). High-angle annular dark-field (HAADF)-EDS mapping verifies the homogeneous dispersion of B, N, and O elements without segregation. The shifted amorphous carbon diffraction peaks indicate altered atomic arrangement of carbon skeletons under varied activation conditions, consistent with XPS findings regarding insufficient or excessive heteroatom doping. Raman spectra (Fig. 3(b)) were adopted to evaluate structural disorder. All samples display distinct D1 (1349 cm^{-1}), D2 (1495 cm^{-1}), D3 (1176 cm^{-1}), and G (1590 cm^{-1}) peaks, corresponding to defective sp^3 carbon, heteroatom-induced defects, out-of-plane carbon atoms, and sp^2 carbon in-plane vibration. The high I_{D1}/I_G ratios (> 1.68) of all

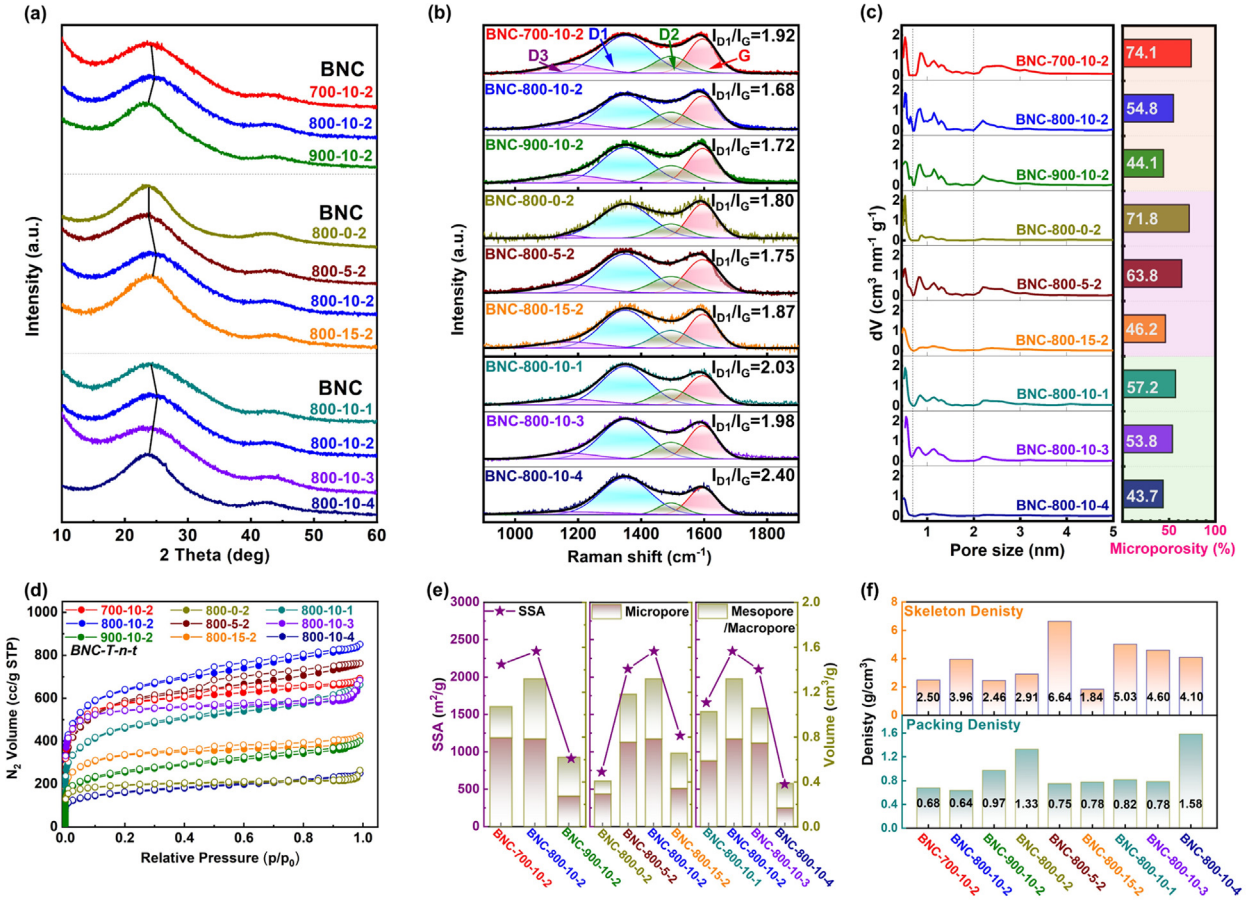

Fig. 3. Structural features of (a) XRD patterns and (b) Raman spectra for BNCs. Textural properties of (c) PSD curves and microporosity, (d) N_2 adsorption-desorption isotherms (solid points represent the adsorption process and the hollow points represent the desorption process), (e) SSA and V_{total}, and (f) skeleton density and packing density for BNCs.

BNCs demonstrate abundant structural defects. The I_{D1}/I_G ratio decreases first and then rises with elevated temperature, activator dosage, and prolonged time. Mild activation etches sp^3 carbon to form pores and improve graphitization, while over-activation destroys sp^2 carbon and increases disorder. Accordingly, moderate activation optimizes the sp^3/sp^2 carbon ratio, constructing favorable porous structures for high hydrogen storage performance.

Activation conditions significantly modulate the textural properties of BNCs. N_2 adsorption-desorption isotherms at 77 K (Fig. 3(d)) reveal combined Type I/IV isotherms for all BNCs, demonstrating hierarchical porous structures. The low-pressure N_2 uptake confirms abundant micropores, while the evident H4 hysteresis loop verifies slit-shaped mesopores and macropores. PSD results (Fig. 3(c), left) further confirm rich ultra-micropores ($\leq$ 0.7 nm) favorable for H_2 adsorption, along with limited supermicropores and mesopores. Microporosity (Fig. 3(c), right) gradually declines with increased activation temperature, activator dosage, and duration. Moderate activation induces partial micropore closure and structural ordering, while intense activation causes carbon skeleton collapse and further micropore loss. The SSA and V_{total} present a volcano-type trend with activation intensity (Fig. 3(e)). Optimized BNC-800-10-2 achieves the maximum SSA (2346.71 m^2/g) and V_{total} (1.32 cm^3/g). Skeletal density varies accordingly, while excessive activation increases packing density (Fig. 3(f)). Such textural evolution comprehensively regulates the gravimetric and volumetric hydrogen storage performance of BNCs (Table S2).

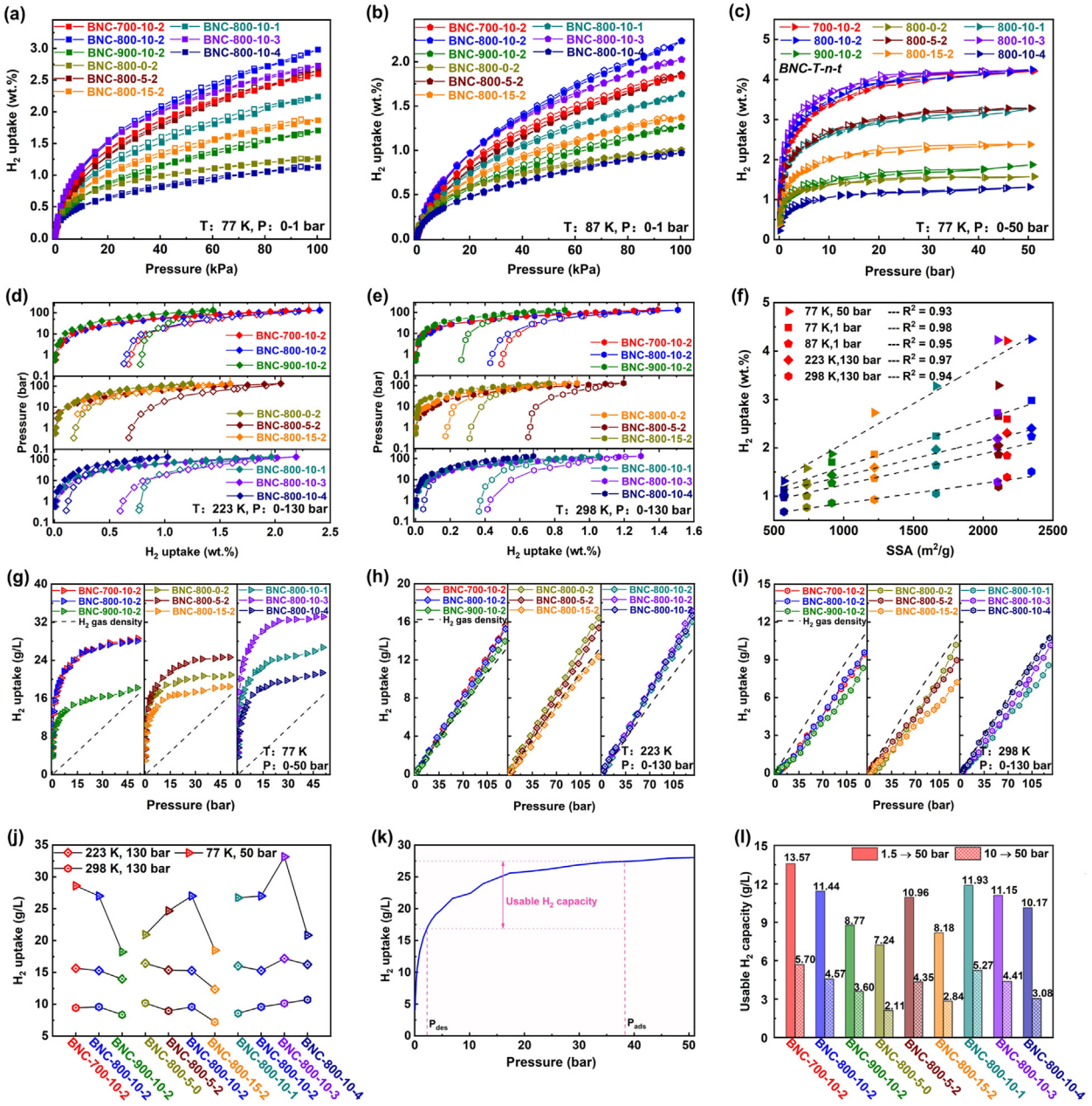

Fig. 4. Gravimetric hydrogen adsorption-desorption isotherms for BNCs at (a) 77 K up to 1 bar, (b) 87 K up to 1 bar, (c) 77 K up to 50 bar, (d) 223 K up to 130 bar, and (e) 298 K up to 130 bar, respectively (solid points represent the adsorption process and the hollow points represent the desorption process). (f) Correlation between total gravimetric hydrogen storage capacity under different test conditions and corresponding SSA. Volumetric hydrogen adsorption isotherms for BNCs at (g) 77 K up to 50 bar, (h) 223 K up to 130 bar, and (i) 298 K up to 130 bar, respectively. (j) Total volumetric hydrogen storage capacity under different test conditions. (k) Schematic of usable hydrogen storage capacity at 77 K and (l) its value at different pressure ranges.

3.3. The effect of activation process on the hydrogen storage performance of BNCs

The hydrogen storage performance of BNCs under different activation conditions was systematically investigated across various temperatures and pressures (Table S3). Low-pressure H_2 adsorption isotherms at 77 and 87 K (Fig. 4(a and b)) exhibit fully reversible and hysteresis-free profiles. Governed by physisorption, the gravimetric hydrogen storage capacity (N_m) declines with rising temperature, ranging from 1.13 wt.% to 2.98 wt.% at 77 K and 0.97 wt.%–2.24 wt.% at 87 K without saturation at 1 bar. High-pressure tests (0–50 bar, 77 K, Fig. 4(c)) show saturated adsorption near 30 bar. Optimally prepared BNC-800-10-2 delivers the maximum N_m of 4.25 wt.%, outperforming insufficiently and excessively activated counterparts. At 223 K and 130 bar (Fig. 4(d)), N_m drops to 1.03 wt.%–2.40 wt.% with obvious desorption hysteresis, revealing deteriorated cycling stability at elevated temperatures. At 298 K (Fig. 4(e)), N_m further decreases to 0.68 wt.%–1.50 wt.%, while BNC-800-10-2 still achieves 1.50 wt.%, exceeding commercial AB_5 alloys [45] and reported porous carbons (Table S4), indicating great promise for on-board hydrogen storage. The stable capacity of 1.5 wt.% after five cycles at room temperature (Fig. S4), together with the linear correlation between N_m and SSA (Fig. 4(f)), verifies the physisorption-dominated storage mechanism.

Volumetric hydrogen storage capacity (N_V) was further evaluated for practical application. At low temperatures, all BNCs possess higher N_V than pure H_2 gas density (Figs. 4(g) and S5), with BNC-800-10-3 reaching the highest N_V of 33.16 g/L at 77 K owing to enhanced packing density. Excessive activation severely reduces low-temperature volumetric performance. With increased testing temperature, the volumetric advantage gradually weakens and completely disappears at 298 K (Fig. 4(h and i)). Activation condition trends (Fig. 4(j)) confirm that harsh activation impairs low-temperature N_V, while prolonged activation slightly improves room-temperature N_V. Practical usable hydrogen capacity was evaluated at 77 K with cutoff desorption pressures (Fig. 4(k and l)) based on reported criteria [46]. BNC-700-10-2 achieves the highest usable capacity of 13.57 g/L (1.5–50 bar) and 5.70 g/L (10–50 bar). Overall, moderately activated BNC-800-10-2 exhibits the optimal comprehensive hydrogen storage performance, whereas excessive activation significantly degrades the gravimetric, volumetric, and usable hydrogen storage capacities of BNCs.

Hydrogen storage capacity depends on the number of adsorbed H_2 molecules, while the isosteric heat of adsorption (Q_{st}) characterizes H_2 adsorption strength, and balancing the two parameters is critical for designing high-performance physisorption materials. Fig. 5(a) depicts the variation of Q_{st} with H_2 coverage. All samples deliver the maximum Q_{st} at near-zero coverage due to the occupation of strong adsorption sites. Activator-free BNC-800-0-2 and over-activated BNCs exhibit higher initial Q_{st} values than optimally activated BNC-800-10-2, which possesses superior storage capacity but relatively low adsorption enthalpy. Consistent with zero-coverage Q_{st}, higher H_2 uptake per SSA is observed in under-activated and over-activated samples (Figs. 5(b①②) and S6, Table S5). With increasing H_2 coverage, Q_{st} declines sharply due to reduced available sites, while larger SSA mitigates this decreasing trend. As shown in Fig. S7, Q_{st} is negatively correlated with the usable H_2 capacity, consistent with the finding that excessive adsorption enthalpy suppresses H_2 desorption and reduces usable capacity in Mg alloy [47]. Therefore, optimization of porous hydrogen storage materials requires a proper balance between H_2 adsorption affinity and usable H_2 capacity. Further correlation analyses (Fig. 5(b③④, c, and d)) demonstrate that Q_{st} has a strong positive correlation with the B/N ratio ($R^2 = 0.85$) but a weak negative correlation with microporosity ($R^2 = 0.62$), with their respective calculated contributions to Q_{st} being 57% and 43%. This indicates that the surface chemical state rather than pore structure dominates the adsorption thermodynamics of BNCs. The regulated B/N ratio enables synergistic B and N co-doping effects, which effectively modulate the intrinsic H_2 adsorption affinity of carbon substrates. The synergistic effect of B and N co-doping was verified by comparing the hydrogen storage performance and H_2 affinity of co-doped BNC-800-10-2, N-doped NC-800-10-2, B-doped BC-800-10-2, and undoped C-800-10-2 under identical activation conditions (Fig. S8). Synthetic schematics of the four samples are shown in Fig. S9, while XRD and Raman data in Fig. S10 confirm their similar carbon skeleton and defect density. XPS spectra (Fig. S11) confirm undoped or mono-doped status for the control samples. BNC-800-10-2 exhibits superior N_m across various temperatures (Fig. S8(a–d)). Even after excluding SSA influence via normalized H_2 uptake and Q_{st} evaluation (Figs. S8(e and f) and S12), BNCs still outperform undoped or mono-doped samples. With no heteroatoms and the lowest microporosity, C-800-10-2 exhibits the smallest microporosity. BC-800-10-2 with lower microporosity and NC-800-10-2 with higher microporosity both show lower Q_{st} than BNC (Fig. S13). Inductively coupled plasma optical emission spectroscopy shows comparable residual Cu contents (0.1 wt.%–0.2 wt.%) for all samples. As reported, Cu at this loading hardly enhances H_2 uptake, so Cu residuals are not the main cause of performance divergence [48]. These results validate the prominent synergistic effect of B

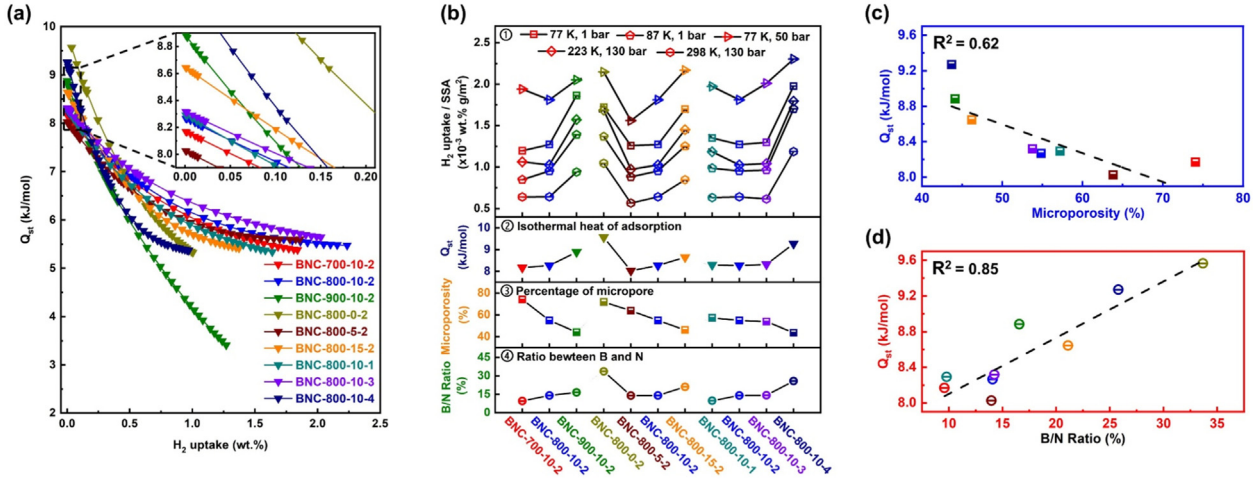

Fig. 5. (a) Evolution of Q_{st} with H_2 coverage; (b) correlation of hydrogen affinity with B/N ratio and microporosity; correlation between Q_{st} and (c) B/N ratio and (d) microporosity for BNCs.

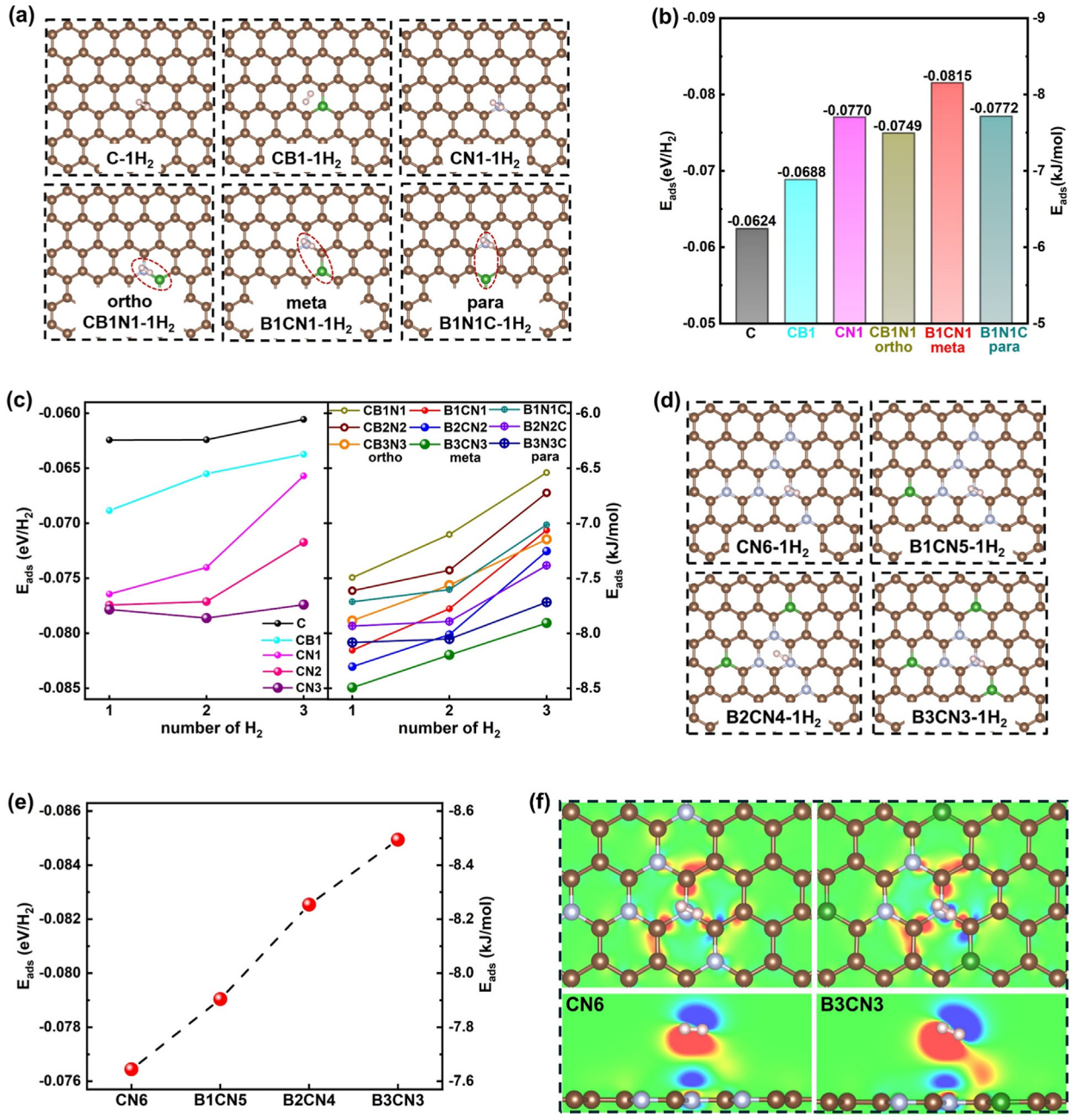

Fig. 6. (a) The adsorption configurations and (b) the diagram of E_{ads} for one H_2 molecule absorbed on C substrates with different doping conditions. (c) The diagram of E_{ads} for varying numbers of H_2 molecules absorbed on C substrates with multiple dopant atoms. (d) The adsorption configurations, (e) the diagram of E_{ads}, and (f) the diagram of charge density difference for one H_2 molecule absorbed on C substrates with a constant total content of B and N but varying B/N ratios (B/N $\leq$ 1).

and N co-doping in strengthening H_2 adsorption behavior. Table S6 compares the performance of BNC–800–10–2 with other reported PCMs. Benefiting from the synergistic effect of B and N co-doping, this sample achieves higher H_2 uptake per SSA than others. As shown in Fig. S14, upon H_2 pressurization, the H_2 pressure and uptake of all samples remain constant with equilibration time, and surface adsorption completes within seconds, demonstrating that the B and N co-doping effect differs from hydrogen diffusion traps in alloys and exerts no influence on sorption kinetics [49].

3.4. Mechanism of H_2 molecules adsorption on B and N co-doped C substrates

DFT calculations were performed to clarify the enhanced H_2 adsorption mechanism of B/N co-doped carbon substrates (Fig. 6(a)). The E_{ads} of single- and co-doped models is substantially higher than that of pristine carbon (Fig. 6(b)), verifying that heteroatom doping strengthens H_2 physisorption. N doping delivers higher E_{ads} than B doping, since electron-rich N centers enhance electrostatic interactions, whereas electron-deficient B atoms offer limited adsorption promotion. Notably, B and N synergistic effects are configuration-dependent: meta-co-doping (B1CN1) achieves superior E_{ads} over single doping and other co-doping modes, while ortho- (CB1N1) and para- (B1N1C) co-doping show inferior or comparable adsorption performance. Multi-H_2 adsorption simulations (Fig. S15, Table S7) demonstrate that E_{ads} gradually declines with increasing H_2 coverage (Fig. 6(c)). Nevertheless, the meta-co-doped configuration maintains the highest E_{ads} under various H_2 coverages. Increasing dopant atom numbers further improves ad-

sorption affinity at a fixed B/N ratio, consistent with experimental findings that the B/N ratio dominates Q_{st} variation. Further simulations with constant total heteroatom content reveal that E_{ads} monotonically increases with the B/N ratio within B/N $\leq$ 1 (Fig. 6(d and e)). The consistent trends of simulated E_{ads} and experimental Q_{st} (Fig. S16) confirm the decisive role of the B/N ratio in regulating H_2 adsorption strength. Charge density difference analysis (Fig. 6(f)) indicates that balanced B and N contents induce prominent surface charge asymmetry via forming B-N structures. This breaks the uniform charge distribution of carbon substrates, creates localized charge defects, and strengthens van der Waals and induced dipole interactions with nonpolar H_2 molecules. Fig. S17 shows that the net Bader charge of the N atom near the H_2 adsorption site on B3CN3 is markedly higher than that of CN6, further supporting this argument. Accordingly, optimizing the B/N ratio effectively enhances charge localization and synergistically boosts the H_2 adsorption capacity of B- and N-co-doped porous carbon.

4. Conclusions

In summary, this study successfully prepared BNCs by the activation process and systematically investigated the effects of activation conditions on their chemical state, microstructure, and hydrogen storage performance. Experimental results demonstrate that BNCs with insufficient or excessive activation exhibit inferior hydrogen storage performance compared to those prepared under optimal conditions. The activation process has dual regulatory effects on both pore texture and elemental doping. While SSA, governed by microstructural evolution, determines the H_2 storage capacity, the B/N ratio within elemental doping primarily dictates H_2 adsorption strength. Specifically, BNC-800-10-2, which has a balance of high SSA (2346.71m^2/g) and B and N co-doping (B/N ratio of 14.07%), achieved a N_m of 4.25 wt.%, a N_V of 33.16 g/L, and a usable H_2 capacity (1.5–50 bar) of 11.44 g/L at 77 K and 50 bar. At 298 K and 130 bar, its N_m reached 1.50 wt.%. In addition, both N_m and Q_{st} (8.27 kJ/mol) of this sample are superior to those (N: 8.03 kJ/mol, B: 6.69 kJ/mol) of samples with single B or N doping under the same activation process. DFT calculations reveal that the E_{ads} of co-doped C substrates is higher than that of single-element doped C substrates, and increasing the B/N ratio further deepens charge defects, thereby enhancing the affinity for H_2 molecules. This study elucidates the critical role of the synergistic effect of B and N co-doping in enhancing H_2 adsorption strength and the importance of balancing doping and high SSA in the preparation of BNCs in achieving excellent hydrogen storage performance.

CRediT authorship contribution statement

Zeming Zhong: Writing – original draft, Conceptualization. **Xue Gao:** Data curation. **Yuchen Mao:** Methodology. **Hui Wang:** Supervision. **Yujun Zhao:** Software. **Lan Zhang:** Validation. **Min Zhu:** Writing – review & editing, Funding acquisition, Conceptualization.

Declaration of competing interest

The authors declare that they have no known competing financial interests or personal relationships that could have appeared to influence the work reported in this paper.

Acknowledgements

This work was supported by the National Key R&D Program of China (No. 2022YFB3803801) and the National Natural Science Foundation of China (No. 52271214).

Supplementary materials

Supplementary material associated with this article can be found, in the online version, at doi:10.1016/j.jmst.2026.11.010.

References

[1] S. Singh, S. Jain, P. Venkateswaran, A.K. Tiwari, M.R. Nouni, J.K. Pandey, S. Goel, Renew. Sustain. Energy Rev. 51 (2015) 623–633.
[2] T. He, P. Pachfule, H. Wu, Q. Xu, P. Chen, Nat. Rev. Mater. 1 (2016) 1–17.
[3] E. Rivard, M. Trudeau, K. Zaghib, Materials 12 (2019) 1973.
[4] L. Zhou, Y. Zhou, Y. Sun, Int. J. Hydrogen Energy 29 (2004) 475–479.
[5] A.W. van den Berg, C.O. Areán, Chem. Commun. (2008) 668–681.
[6] Q. Lai, Y. Sun, T. Wang, P. Modi, C. Cazorla, U.B. Demirci, J.R. Ares Fernandez, F. Leardini, K.F. Aguey-Zinsou, Adv. Sustain. Syst. 3 (2019) 1900043.
[7] Y. Gogotsi, R.K. Dash, G. Yushin, T. Yildirim, G. Laudisio, J.E. Fischer, J. Am. Chem. Soc. 127 (2005) 16006–16007.
[8] Z. Geng, C. Zhang, D. Wang, X. Zhou, M. Cai, J. Energy Chem. 24 (2015) 1–8.
[9] R. Härmas, R. Palm, M. Russina, H. Kurig, V. Grzimek, E. Härk, M. Koppel, I. Tallo, M. Paalo, O. Oll, J. Embs, E. Lust, Carbon 155 (2019) 122–128.
[10] M. Tian, M.J. Lennox, A.J. O'Malley, A.J. Porter, B. Krüner, S. Rudić, T.J. Mays, T. Düren, V. Presser, L.R. Terry, S. Rols, Y. Fang, Z. Dong, S. Rochat, V.P. Ting, Carbon 173 (2021) 968–979.
[11] F. Fan, J. Ren, Y. He, X. Chen, Res. Phys. 46 (2023) 106263.
[12] P. Chen, X. Wu, J. Lin, K.L. Tan, Science 285 (1999) 91–93.
[13] X. Sun, L. Gu, Y. Lu, Q. Luo, B. Hu, J. Li, C. Wu, Y. Zhang, Q. Gu, Q. Li, Nat. Commun. 17 (2026) 6634.
[14] T.K. Hoang, D.M. Antonelli, Adv. Mater. 21 (2009) 1787–1800.
[15] S. Liu, J. Liu, X. Liu, J.-X. Shang, R. Yu, J. Shui, Appl. Phys. Rev. 9 (2022) 021315.
[16] W. Qiao, W. Liu, D. Yin, N. Ding, Y. Liu, H. Sun, Y. Wang, Z. Wang, C. Wang, L. Wang, J. Yuan, Y. Cheng, Nano Res. Energy 5 (2026) e9120216.
[17] I. Rossetti, G. Ramis, A. Gallo, A. Di Michele, Int. J. Hydrogen Energy 40 (2015) 7609–7616.
[18] D.S. Pyle, E.M. Gray, C.J. Webb, Int. J. Hydrogen Energy 41 (2016) 19098–19113.
[19] M. Li, W. Yin, J. Pan, Y. Zhu, N. Sun, X. Zhang, Y. Wan, Z. Luo, L. Yi, L. Wang, Chem. Eng. J. 471 (2023) 144691.
[20] Y. Jeong, T.C.M. Chung, Carbon 49 (2011) 140–146.
[21] M. Sankaran, B. Viswanathan, Carbon 44 (2006) 2816–2821.
[22] Z.H. Zhu, H. Hatori, S.B. Wang, G.Q. Lu, J. Phys. Chem. B 109 (2005) 16744–16749.
[23] I.K. Petrushenko, K.B. Petrushenko, Surf. Interfaces 17 (2019) 100355.
[24] K.Y. Kang, B.I. Lee, J.S. Lee, Carbon 47 (2009) 1171–1180.
[25] L. Wang, R.T. Yang, J. Phys. Chem. C 113 (2009) 21883–21888.
[26] S. Giraudet, Z. Zhu, Carbon 49 (2011) 398–405.
[27] X. Gao, L. Hu, Y. Mao, Z. Zhong, L. Huang, K. Xia, H. Wang, M. Zhu, J. Phys. Chem. C 127 (2023) 24027–24038.
[28] A. Rehman, S.-J. Park, Carbon 159 (2020) 625–637.
[29] A. Rehman, G. Nazir, K. Heo, S. Hussain, M. Ikram, Q. Mahmood, T. Alshahrani, H.S.M. Abd-Rabboh, J. Energy Storage 66 (2023) 107468.
[30] M. Endo, T. Hayashi, S.-H. Hong, T. Enoki, M.S. Dresselhaus, J. Appl. Phys. 90 (2001) 5670–5674.
[31] Y. Ferro, F. Marinelli, A. Jelea, A. Allouche, J. Chem. Phys. 120 (2004) 11882–11888.
[32] L. Firlej, B. Kuchta, K. Walczak, C. Journet, Nanomaterials 11 (2021) 2173.
[33] T.C.M. Chung, Y. Jeong, Q. Chen, A. Kleinhammes, Y. Wu, J. Am. Chem. Soc. 130 (2008) 6668–6669.
[34] A. Qajar, B.M. Holbrook, M. Peer, R. Rajagopalan, H.C. Foley, M. Davis, K.T. Mueller, Carbon 89 (2015) 392–403.
[35] Z. Chen, L. Hou, Y. Cao, Y. Tang, Y. Li, Appl. Surf. Sci. 435 (2018) 937–944.
[36] A. Morandé, P. Lillo, E. Blanco, C. Pazo, A.B. Dongil, X. Zarate, M. Saavedra-Torres, E. Schott, R. Canales, A. Videla, N. Escalona, J. Energy Storage 64 (2023) 107193.
[37] T. Kopac, Y. Kırca, Int. J. Hydrogen Energy 45 (2020) 10494–10506.
[38] L. Wang, F.H. Yang, R.T. Yang, AIChE J. 55 (2009) 1823–1833.
[39] M. Pizzochero, O. Leenaerts, B. Partoens, R. Martinazzo, F.M. Peeters, J. Phys.: Condens. Matter 27 (2015) 425502.
[40] J. Peng, X. Dai, J. Huang, J. Zeng, L. Zheng, H. Chen, J. Energy Storage 59 (2023) 106498.
[41] J. Huang, J. Peng, J. Zeng, L. Zheng, H. Chen, J. Energy Storage 87 (2024) 111514.
[42] Y. Sun, P.A. Webley, Chem. Eng. J. 162 (2010) 883–892.
[43] L. Czepirski, J. JagieŁŁo, Chem. Eng. Sci. 44 (1989) 797–801.
[44] Z. Shen, Y. Song, C. Yin, X. Luo, Y. Wang, X. Li, Microporous Mesoporous Mater. 322 (2021) 111158.
[45] C. Qian, H. Du, H. Wang, Rare Met. Mater. Eng. 1 (2000) 25–27.
[46] M. Schlichtenmayer, M. Hirscher, Appl. Phys. A 122 (2016) 379.
[47] Y. Zheng, S. Yang, B. Hu, Y. Lu, Y. Yang, K. Tang, Q. Luo, B. Liu, Q. Li, F. Pan, J. Magnes. Alloy 13 (2025) 2959–2977.
[48] G. Conte, A. Policicchio, O. De Luca, P. Rudolf, G. Desiderio, R.G. Agostino, Int. J. Hydrogen Energy 47 (2022) 18384–18395.
[49] X. Sun, X. Yang, Y. Lu, Q. Luo, C. Wu, Y. Zhang, T. Lyu, Q. Gu, Q. Li, F. Pan, J. Mater. Sci. Technol. 202 (2024) 119–128.